

This document is the accepted manuscript version of the following article:

Priebe, A., Barnes, J. P., Edwards, T. E. J., Huszár, E., Pethö, L., & Michler, J. (2020). Elemental characterization of Al nanoparticles buried under a Cu thin film - TOF-SIMS vs. STEM/EDX. *Analytical Chemistry*. <https://doi.org/10.1021/acs.analchem.0c02361>

## Elemental characterization of Al nanoparticles buried under a Cu thin film – TOF-SIMS vs. STEM/EDX

Agnieszka Priebe<sup>1,\*</sup>, Jean-Paul Barnes<sup>2</sup>, Thomas Edward James Edwards<sup>1</sup>, Emese Huszár<sup>1</sup>, Laszlo Pethö<sup>1</sup> and Johann Michler<sup>1</sup>

<sup>1</sup>Empa, Swiss Federal Laboratories for Materials Science and Technology, Laboratory for Mechanics of Materials and Nanostructures, Feuerwerkerstrasse 39, CH-3602 Thun, Switzerland

<sup>2</sup>Univ. Grenoble Alpes, CEA, LETI, 38000 Grenoble

\*Corresponding author: [agnieszka.priebe@empa.ch](mailto:agnieszka.priebe@empa.ch)

**ABSTRACT** In this work we present a comprehensive comparison of Time-of-Flight Secondary Ion Mass Spectrometry (TOF-SIMS) and Scanning Transmission Electron Microscope combined with Energy-Dispersive X-ray Spectroscopy (STEM/EDX), which are currently the most powerful elemental characterization techniques in the nano- and micro-scale. The potential and limitations of these methods are verified using a novel dedicated model sample consisting of Al nanoparticles buried under a 50 nm thick Cu thin film. The sample design based on the low concentration of nanoparticles allowed us to demonstrate the capability of TOF-SIMS to spatially resolve individual tens of nanometre large nanoparticles under Ultra-High Vacuum (UHV) as well as High Vacuum (HV) conditions. This is a remarkable achievement especially taking into account the very small quantities of the investigated Al content. Moreover, the imposed restriction on the Al nanoparticles location, i.e. only on the sample substrate, enabled us to prove that the measured Al signal represents the real distribution of Al nanoparticles and does not originate from the artefacts induced by the surface topology. The provided comparison of TOF-SIMS and STEM/EDX characteristics delivers guidelines for choosing the most optimal method for efficient characterization of nano-objects.

**KEYWORDS:** nanoparticles, elements, chemical structure, chemical characterization, TOF-SIMS, STEM/EDX

### INTRODUCTION

The application scope of nanoparticles has been enlarging over recent decades as they offer new possibilities, which are usually not attainable in the case of their macroscopic equivalents. For example, Ag nanoparticles have excellent antibacterial<sup>1</sup>, antifungal<sup>2</sup> and antiviral<sup>3</sup> properties. Moreover, they are used in medical instrumentation<sup>4</sup>, biosensors<sup>5</sup>, fabrics<sup>6</sup> and electronics (i.e. piezoelectric energy harvesters<sup>7</sup>, antennas and sub-THz metamaterials<sup>8</sup>, as ink for metallic micropatterns<sup>9</sup> and highly conductive LED devices<sup>10</sup>). Au nanoparticles find applications in medicine, such as breast cancer detection and therapy<sup>11</sup>, enhancers of DNA signals during Raman spectroscopy<sup>12</sup>, in cell detection and labelling<sup>13</sup>, protein<sup>14</sup> and heavy metals<sup>15,16</sup> detection and glucose sensors for diabetics<sup>17</sup>. ZnO nanoparticles<sup>18</sup> and TiO<sub>2</sub> nanoparticles<sup>19</sup> have potential for cancer treatment and are used in sunscreens<sup>20</sup>. SiO<sub>2</sub> nanoparticles can improve mechanical properties of bio-nanocomposites used for food packaging<sup>21</sup>. Fuel catalysts based on CeO<sub>2</sub> nanoparticles were found to reduce diesel fuel consumption and therefore green-house gas emissions<sup>22</sup>. In summary, the presence of nanoparticles in daily life has become almost unavoidable.

The properties and functionality of nanoparticles are strongly dependent on their size, shape, chemical composition, nanostructure and their environment. Moreover, potential toxicity and response of living organisms to omnipresent nanoparticles remain partly

an open question. This implies a strong need for proper elemental characterization techniques, which allow nanoparticle-containing systems to be represented in two- or three-dimensional spaces.

In this work, a novel dedicated model sample based on Al nanoparticles buried under a 50 nm thick Cu thin film was used to explore the potential and limitations of two, currently the most powerful techniques, i.e. Time-of-Flight Secondary Ion Mass Spectrometry (TOF-SIMS)<sup>23,24</sup> and Scanning Transmission Electron microscopy combined with Energy Dispersive X-ray spectroscopy (STEM/EDX)<sup>25,26</sup>, which allow a sample chemical structure to be characterized with nanometre scale resolution. The model sample was designed in such a way to prove the capability of TOF-SIMS to spatially resolve individual nanoparticles, which was the main concern of our previous studies<sup>27</sup> conducted on Al nanoparticles distributed in a Bulk Metallic Glass (BMG<sup>28</sup>; ZrCuAg). Therefore, a low concentration of Al nanoparticles in a strictly defined location, i.e. only directly on a sample substrate, was ensured. Besides, the verification on whether a nanoparticle signal detected with TOF-SIMS represents a real Al distribution or results from sample topology-induced artefacts was addressed in this study. Al nanoparticles were chosen mainly due to the excellent ionization efficiency of Al and low detection limits<sup>29</sup> which make them an excellent candidate for studying TOF-SIMS resolution limits. Besides, Al nanoparticles have very promising properties

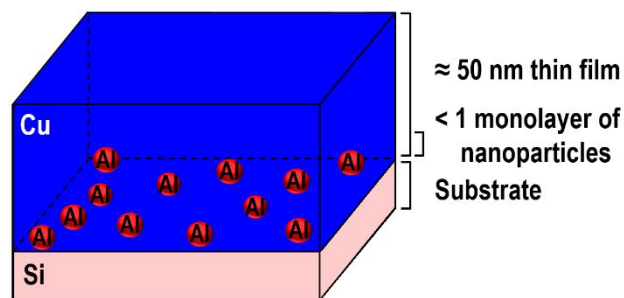


Figure 1. Diagram of the model sample for verifying TOF-SIMS potential to characterize nano-objects. Not to scale.

for Si solar cells<sup>30</sup>, thin-film GaAs photodiodes<sup>31</sup>, thin-film GaAs photodiodes<sup>31</sup>, plasmon-enhanced solar desalination systems<sup>32</sup>, light-emitting devices (LED)<sup>33</sup> and additives for diesel fuel (as they improve ignition probability<sup>34</sup>). Therefore, the results presented in this work demonstrate the application scope of TOF-SIMS for microelectronics and new energy devices.

## EXPERIMENTAL PART

### Materials

A dedicated model sample composed of Al nanoparticles buried under an around 50 nm thick Cu thin film (Figure 1) was designed and fabricated at Empa. The sample components were chosen to ensure a high mass contrast (the mass to charge ratio for aluminium is  $\left(\frac{m}{Q}\right)_{Al}=27$  and for copper is  $\left(\frac{m}{Q}\right)_{Cu}=63$ ) and prevent potential mass interference during a TOF-SIMS analysis. The main advantage of Al in this case is its high ion yield and low detection limit ( $3 \times 10^8$  atoms/cm<sup>2</sup>), i.e. two orders of magnitude lower than the detection limit of Cu ( $3 \times 10^{10}$  atoms/cm<sup>2</sup>) on a Si wafer substrate<sup>29</sup>. Moreover, aluminum has a high affinity to oxygen which leads to the formation of native aluminium oxide on the surface<sup>35</sup>. This is very beneficial as oxygen enhances positive ion yields<sup>24,36,37</sup> and, therefore, an oxide shell is expected to increase the generation of Al secondary ions. The thickness of such oxide layers is in the order of several nanometers and depends on crystallographic orientation, temperature and pressure<sup>38–42</sup>. For example, aluminum oxide thickness at room temperature and ambient pressure is around 3–4 nm<sup>39,43</sup>. This range is in good agreement with calculations based on the thermodynamical model<sup>40</sup>. Variable charge molecular-dynamics simulations of the Al nanocluster oxidation show that a stable 4 nm thick amorphous oxide is formed during less than 470 ps simulation time<sup>44</sup> which is much shorter than the deposition process of the model sample presented in this study. The oxidation process, however, can be significantly slower as presented in the case of monocrystalline Ag nanoparticles, which showed stability in the timescale of approx. one month<sup>45</sup>. In summary, the low Al detection limit in conjunction with the oxygen content have increased the probability of spatially resolving the nanoparticles in 3D using TOF-SIMS. Besides, the Al and Cu characteristic lines are well separated ( $K_{\alpha,Al}=1.486$  keV,  $K_{\alpha,Cu}=8.040$  keV and  $L_{\alpha,Cu}=0.930$  keV) which allows peak overlaps in EDX spectra to be avoided.

The deposition parameters were adjusted to generate less than one monolayer of tens of nanometer large Al

nanoparticles on a Si substrate. This condition was imposed to obtain individual nanoparticles and prevent formation of nanoparticle agglomerates/clusters. The Cu layer was incorporated using a Physical Vapour Deposition (PVD) technique<sup>46</sup> around 30 min after the deposition of nanoparticles to enable the surface of the Al nanoparticles to oxidize.

Figure S1 (in Supporting Information) shows a diagram of an Ultra-High Vacuum (UHV) custom-made instrument which was used for the sample preparation. A sputter magnetron<sup>47,48</sup> was used for sputtering the Cu layer and a NanoGen50 nanoparticle source from MANTIS Deposition Ltd. (Oxfordshire, United Kingdom) was used for the synthesis of Al nanoparticles. 99.99% purity Al and Cu targets were supplied by HMW Hauner GmbH & Co. KG (Roettenbach, Germany). The sample was deposited on a <100> single crystal Si substrate rotated at 5 rpm at room temperature, and the sample holder was on ground potential. The base pressure prior to the deposition was  $5.7 \times 10^{-7}$  mbar. 15 sccm Ar flow was supplied to the magnetron and 100 sccm Ar flow was supplied to the aggregation zone giving  $3 \times 10^{-3}$  mbar process pressure near the substrate surface. The nucleation of Al nanoparticles was obtained at the process pressure up to one order of magnitude higher inside the aggregation zone. The cooling jacket provided temperature of 29° on the external part of the aggregation zone. The generated charged nanoparticles were measured using a quadrupole mass spectrometer (Figure S2). The magnetron in NanoGen50 was driven by 175 mA direct current (DC) power source. 233 V plasma potential resulted in 41 W average power. The magnetron used for sputtering the Cu thin film operated at 200 mA, DC source. In this case 471 V potential provided 94 W average power.

Depositing a sub-monolayer of Al nanoparticles lasted 45 minutes, which was followed by a 30 min break to ensure Al nanoparticle surface oxidation. Subsequently, the Cu thin film was deposited on top of the Al nanoparticles with a deposition rate of 0.147 nm/s within 5.7 min. Thus, the entire deposition process took less than 1.5 hour.

Additionally, before a sample lift-out<sup>37,49</sup> for STEM/EDX measurements on the sample cross-section the sample surface was coated with a platinum protective layer to prevent the Focused Ion Beam (FIB<sup>50</sup>)-induced surface destruction/modification.

### Methods

A sample elemental characterization was conducted using a dedicated UHV (Ultra-High Vacuum) dual-beam instrument TOF.SIMS<sup>5</sup> from IONTOF (Munich, Germany). A Bi<sub>3</sub><sup>2+</sup> beam served as an analysis beam and an O<sub>2</sub> beam was used for sputtering. The 60 keV pulsed 0.04 pA (0.5 nA DC and 200 ns pulse length) Bi<sub>3</sub><sup>2+</sup> beam with 60 μs cycle time and 10 shots/pixel scanned in the high resolution mode over a 5 μm×5 μm Region-Of-Interest (ROI) with a 512 pixels×512 pixels raster size. A sawtooth raster mode and primary ion flight time correction were applied. The 500 eV energy and 67 nA DC O<sub>2</sub> beam scanned over 200 μm×200 μm area. Oxygen flooding ( $3.7 \times 10^{-6}$  mbar O<sub>2</sub> pressure) was additionally provided to enhance positive ion generation. 106 scans were acquired over approximately 4 hours 38 minutes.

In order to validate the TOF-SIMS potential for imaging nanoparticles under HV (High Vacuum) conditions, the measurements were repeated with an upgraded HV-compatible prototype of compact TOF (CTOF) from TOFWERK (Thun, Switzerland) which was integrated within a FIB/SEM (Focused Ion Beam/Scanning Electron Microscope) multi-analytical instrument from Tescan (Brno, Czech Republic). Compared to the previous models of CTOF detectors, this prototype has an improved ion extraction and transfer optics which, in a conjunction with a better vacuum system and more precise stage positioning, allows the measured secondary ion signal to be significantly increased and the background noise in mass spectra to be reduced. Therefore, the operation at much lower primary ion beam currents, and consequently lower beam spot size, is possible. A continuous mono-isotopic  $^{69}\text{Ga}^+$  primary beam at 30 keV energy and 4 pA ion current was used for both sputtering and analysis. The data was acquired in the positive ion detection mode from a  $5\text{ }\mu\text{m} \times 5\text{ }\mu\text{m}$  ROI with  $1024 \times 1024$  pixels and  $2 \times 2$  binning (this provides the same pixel size of 9.77 nm as the one applied during the measurements with TOF.SIMS<sup>5</sup>) at 10  $\mu\text{s}$  dwell time. The aperture of 50  $\mu\text{m}$  was used. 159 frames were recorded in less than 28 minutes.

The TOF-SIMS mass spectra were mass calibrated using the most prominent isotopes of the thin film ( $^{27}\text{Al}^+$  and  $^{63}\text{Cu}^+$ ), the substrate ( $^{28}\text{Si}^+$ ) and the primary beam (either  $^{209}\text{Bi}^+$  or  $^{69}\text{Ga}^+$ ).

The lamella for cross-sectional imaging and analysis of the thin film composite were produced by FIB lift-out process on a Helios NanoLab FIB/SEM tool from FEI (Hillsboro, OR, USA) using a Mo support. The lamellar thickness was  $124 \pm 2$  nm. Titan Themis TEM from FEI (Hillsboro, OR, USA) was used to measure the precise size of the Al nanoparticles. The high-angle annular dark-field (HAADF) images (0.82 nm pixel size) from 66–200 mrad range were recorded at 300 keV energy electron beam in STEM mode. A SuperEDX system at 5.3 nA and 10  $\mu\text{s}$  dwell time was used to generate chemical maps. These images were obtained from an area of  $619\text{ nm} \times 206\text{ nm}$  as a series of 550 drift-corrected and integrated frames. In this case, the entire measurement procedure took around 4 hours, which includes around 2 hours for the sample lift-out and around 2 hours for the actual TEM measurement.

## RESULTS AND DISCUSSION

### *3D elemental characterization using TOF-SIMS under UHV base pressure conditions*

Figure 2 shows a 3D elemental representation of the Al nanoparticles buried under the 50 nm thick Cu thin film deposited on the Si substrate. The data were obtained with  $\text{Bi}_3^{2+}$  using TOF.SIMS<sup>5</sup>.  $^{63}\text{Cu}^+$  and  $^{28}\text{Si}^+$  signal distributions are uniform over the entire ROI, whilst distinct  $^{27}\text{Al}^+$  signal segregation indicates a spatially resolved detection of single Al nanoparticles. This is a great achievement taking into account the very small amount of Al content in the sample. In this case, the exact size of the nanoparticles cannot be reliably assessed. Due to the size of the imaging ion beam (i.e. around 50–60 nm), which most likely is greater than the size of the nanoparticles, the measured shape and size of

nanoobjects represent rather convolutions of the nanoparticles and the primary ion beam.

A 3D chemical imaging provides detailed information on the distributions of various elements in a sample. However, in order to judge on a global tendency in a sample structure, the depth profiling can be much more informative. In this type of elemental data representation, an isotope signal is averaged over a chosen volume and shown as a function of sputtering time, the number of acquired scans or the sample depth. The latter is only possible when a material sputtering rate is known (this is usually not applicable in the case of novel materials) or when a crater depth was measured with AFM (Atomic Force Microscope<sup>31</sup>) or SEM after the TOF-SIMS measurement. Usually the depth profiles are generated from the central part of a measured region, i.e. the margins with a 25% reduced scan width are excluded from an analysis to avoid influence of edge artefacts such as material re-deposition or drift-induced image shifts.

The depth profiles obtained from the central  $2.5\text{ }\mu\text{m} \times 2.5\text{ }\mu\text{m}$  region of Figure 2 are given in Figure S3 and 3. A proper estimation of an interface location between an exact sample and a sample substrate is crucial for the correct data interpretation. Usually, it is indicated by a cross-point between two signal distributions of the most prominent ions/isotopes composing a sample and a substrate. However, in the case when one of the signals is too low, an interface location can be assumed to be at 50% of an ascending scope of the substrate signal distribution. In the normalized to 1 TOF-SIMS depth profiles of the Al nanoparticle-containing Cu thin film (Figure 3),  $^{27}\text{Al}^+$  and  $^{63}\text{Cu}^+$  signal distributions do not cross the  $^{28}\text{Si}^+$  signal distribution at the same time (which is expected when Al nanoparticles do not cover the entire Si substrate and the space between them as well as the space between the spherical nanoparticles and the substrate is filled with Cu). Since the  $^{63}\text{Cu}^+ - ^{28}\text{Si}^+$  distribution cross point appears at around 50% of the maximum  $^{28}\text{Si}^+$  signal, it seems more likely that the exact interface starts after around 3700 s of sputtering time than after around 5100 s (i.e. the location of  $^{27}\text{Al}^+ - ^{28}\text{Si}^+$  cross-point). The interface spread (marked in pink) has the width of around 1400 s and can be explained with different sputtering rates of the sample components (as presented in Figure 4). According to Yamamura model<sup>32</sup> for the applied primary  $\text{Bi}_3^{2+}$  beam parameters (i.e. 60 keV energy and  $45^\circ$  incident angle), roughly estimated Al, Cu and Si sputter yields<sup>34</sup> are  $Y_{\text{SP,Al}} = 14.13$ ,  $Y_{\text{SP,Cu}} = 25.70$  and  $Y_{\text{SP,Si}} = 7.20$ , respectively (source: SurfaceLab 6.5 software from IONTOF). This means that Al sputters almost twice as slow as Cu and almost twice as fast as Si. Moreover, as it was already mentioned, the Al nanoparticle surface is covered with spontaneously forming  $\text{Al}_2\text{O}_3$  layer. Although, the thickness of such a shell is expected to only be up to several nanometers, this constitutes a relatively large fraction of tens of nanometer large nanoparticles (see the TEM results, Figure 7) and can significantly decrease the milling efficiency. In conclusion, the sputtering process is not uniform over the entire ROI and can lead to the formation of primary ion beam-induced roughness. The increased secondary ion signals of all elements within the first 235 s of sputtering time most likely result from the sample surface oxidation as oxygen is a very well-known element for enhancing positive ion yields. In the

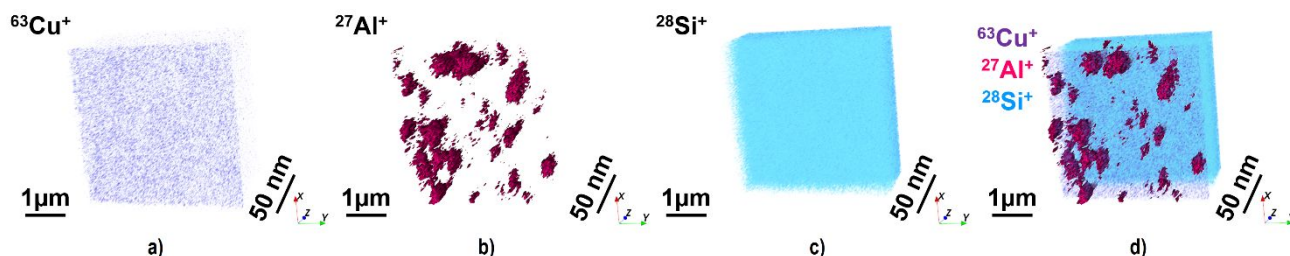


Figure 2. 3D representation of Al nanoparticles buried under approximately 50 nm thick Cu layer: secondary ion signal distributions of  $^{63}\text{Cu}^+$  (a),  $^{27}\text{Al}^+$  (b),  $^{28}\text{Si}^+$  (c) and their overlay (d). Al signal iso-surface was obtained using the median filter with kernel size = 3 and 11.1% signal threshold. The results were obtained with the 60 keV  $\text{Bi}_3^{2+}$  beam using TOF.SIMS<sup>5</sup> instrument.

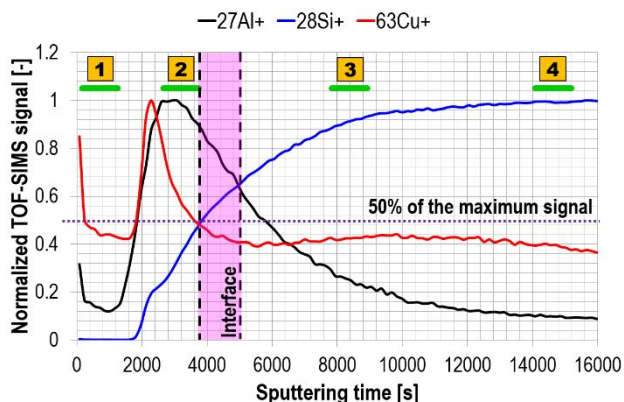


Figure 3. Normalized to 1 TOF-SIMS depth profiles of Al nanoparticles buried under Cu thin film acquired with  $\text{Bi}_3^{2+}$  beam from the  $2.5\ \mu\text{m} \times 2.5\ \mu\text{m}$  ROI of Figure 2. The green lines represent signal integration times used for generating elemental images given in Figure 5. The pink stripe denotes the estimated interface spread between the Al nanoparticle-containing Cu thin film and the Si substrate.

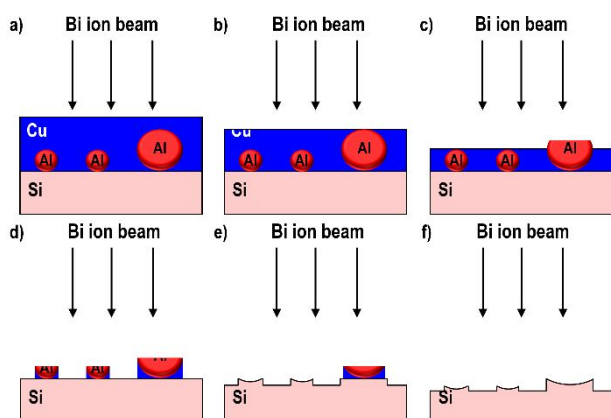


Figure 4. Schematic interpretation of the measured interface spread in TOF-SIMS depth profiles. A) the initial sample structure, b) milling through the pure Cu layer, c-d) due to the different sputtering rates of Al, Cu and e-f) Si, the nanoparticles, the thin film layer and the substrate are non-uniformly milled by a primary ion beam.

case of Cu, the highest ionization efficiency was recorded close to the  $^{27}\text{Al}^+$  signal peak (the Cu signal was 15% higher than the Cu peak signal measured at the surface). This indicates high sensitivity of Cu ionization not only to the presence of oxygen atoms but also Al and/or Si (i.e. matrix effect). The maximum of  $^{27}\text{Al}^+$  signal appears close to the interface with the substrate (at 2910 s sputtering time) where actual nanoparticles were expected. The other Al peak measured close to the sample surface is 68% lower and significantly narrower. This can indicate

diffusion of Al atoms (rather than entire nanoparticles) to the surface region. On the other hand, it has to be taken into account that the Al detection limit is very low, i.e. two orders of magnitude lower than the Cu detection limit<sup>29</sup>. Therefore, this peak can simply originate from a trace amount of Al whose excellent ionization probability was additionally increased by oxygen.

The TOF-SIMS technique is based on measuring the time which an ion needs to cover a certain distance. The second power of this time is proportional to the  $m/Q$  ratio and, therefore, allows for element recognition. However, more than one ion (either an ionized atom or an ionized molecule) in a sample can have the same (or very similar)  $m/Q$ , which can lead to mass interference and introduce artefacts to the data analysis. In the case of the studied model sample, the elements were chosen in such a way that the probability of mass interference was reduced. Nevertheless, to verify the presence of mass interference, the measured isotope abundance was compared to the natural isotope abundance. For single-isotope elements, such as Al, this comparison is not possible but Al is the lightest element in the sample. Thus, hypothetically it can only mass interfere with residual gas molecules such as C, N and O. However, these ions usually appear in the negative ion detection mode and are rather not expected to be measured among positive ions. The measured isotope abundance of Cu perfectly follows the values of natural isotope abundance (i.e. 69.1%  $^{63}\text{Cu}^+$  and 30.9%  $^{65}\text{Cu}^+$ ), therefore in this case the mass interference can be excluded. Deviations up to 4% were observed for Si (88.2%  $^{28}\text{Si}^+$ , 8.6%  $^{29}\text{Si}^+$  and 3.2%  $^{30}\text{Si}^+$  of measured values versus 92.2%  $^{28}\text{Si}^+$ , 4.7%  $^{29}\text{Si}^+$  and 3.1%  $^{30}\text{Si}^+$  of expected values) which most likely results from the mass interference with Al-containing ions (i.e.  $^{27}\text{Al}^+\text{H}^+$  and  $^{27}\text{Al}^+\text{H}_2^+$ ). This mass interference can explain the presence of a small (around 290 times lower than the  $^{28}\text{Si}^+$  maximum signal value) local  $^{28}\text{Si}^+$  peak in the proximity to the sample surface in the Si depth profile (Figure S3).

Sample topology can significantly influence TOF-SIMS signals<sup>37,53</sup> leading to imaging artefacts. Despite certain indications, such as a repetitive increase of a signal on one side of 3D objects (such as grains or cracks), not always is it possible to distinguish the chemical component from the morphological one. The SEM imaging (Figure S4) shows the presence of bright round objects on the surface of the model sample, which most likely result from Al nanoparticles covered with the Cu layer. In order to verify the impact of the surface roughness on the  $^{27}\text{Al}^+$  secondary ion signal distribution measured with TOF-SIMS, 2D chemical maps at different depths (marked with green lines in Figure 3) were



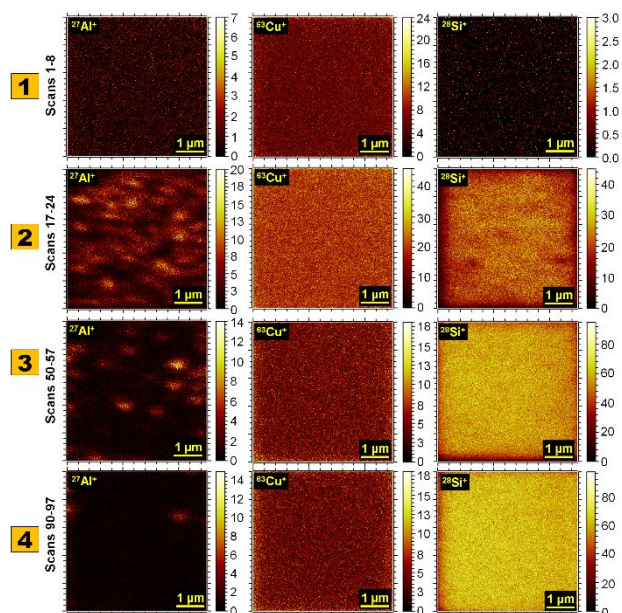


Figure 5. Elemental distribution of the main sample isotopes ( $^{27}\text{Al}^+$ ,  $^{63}\text{Cu}^+$  and  $^{28}\text{Si}^+$ ) acquired with  $\text{Bi}_3^+$  beam at different depths of the sample (marked in Figure 3).

integrated over the same sputtering time (i.e. 8 scans; Figure 5). Region 1 represents a near-surface region of the Cu layer. In this part of the thin film Al nanoparticles were not expected and, indeed,  $^{27}\text{Al}^+$  signal segregation is not observed there. In the conjunction with Figure 3 showing the significantly increased  $^{27}\text{Al}^+$  signal in the proximity of the sample surface, this seems to confirm the diffusion of Al atoms towards the sample surface during and/or after the deposition process takes place. Al nanoparticle signal variations were well discriminated in region 2. Despite that,  $^{63}\text{Cu}^+$  signal distribution was uniform, meaning no  $^{63}\text{Cu}^+$  signal deficiency due to the presence of Al nanoparticles. This is in contrast to the STEM/EDX results (Figure 7) and most likely results from an insufficient secondary ion count rate. However, it has to be also kept in mind that although Al nanoparticles are present in this region, the Cu atoms constitute the majority of the thin film volume. Besides, the comparison of the  $^{27}\text{Al}^+$  and  $^{63}\text{Cu}^+$  depth profiles (Figure S3) shows that on average  $^{63}\text{Cu}^+$  signal is only 1.7 times higher than  $^{27}\text{Al}^+$  signal at this location despite the dominant contribution of Cu to the sample composition. This demonstrates that the generation of Al secondary ions is much more efficient than the generation of Cu secondary ions. A near-interface substrate section and a deep substrate section are presented in regions 3 and 4, respectively. In both cases, Al signal was still present, most likely due to the different sputter rates between Al and Si (as shown in Figure 4). Nevertheless, the corresponding  $^{27}\text{Al}^+$  and  $^{28}\text{Si}^+$  signal distributions indicate that the potential mass interference between  $^{28}\text{Si}^+$  and  $^{27}\text{Al}^+\text{H}^+$  has a negligible effect on  $^{28}\text{Si}^+$  signal distribution in these 2D images (no similarities in image patterns can be distinguished). Moreover, primary ion beam-induced roughness seems to be irrelevant to the image quality in this case. In summary, Figure 5 proves that the acquired segregation of  $^{27}\text{Al}^+$  signal in Figure 2 represents real elemental distribution of Al nanoparticles and does not result from the artefacts induced by the surface topology.

### Elemental imaging with TOF-SIMS at HV conditions with $\text{Ga}^+$ beam

Among all secondary species, which are ejected by a primary ion beam, only a small fraction is ionized and can be detected. Therefore, an efficient ion collection is particularly important in the case of TOF-SIMS technique and the dedicated instruments (such as TOF.SIMS<sup>5</sup>) operate at UHV conditions. However, a need of conducting correlative and/or complementary analysis of a specimen (for example *in situ* TOF-SIMS and EDX measurements of elemental structure, topology measurements obtained with SEM, crystallographic orientation measurements with Electron BackScatter Diffraction, EBSD or surface roughness analysis with AFM, all conducted without breaking vacuum conditions) resulted in developing HV-compatible TOF-SIMS detectors<sup>54</sup>. Comparing HV and UHV conditions, two parameters have to be taken into account, i.e. the mean free path and the time needed for a single monolayer formation.

The mean free path,  $L$  (given in m), is defined as an average distance covered by a molecule between collisions and is determined in air at room temperature (20°C) by the pressure,  $p$  (given in mbar), in an analytical chamber<sup>55,56</sup>:

$$L \approx \frac{6.62 \times 10^{-5}}{p}. \quad (1)$$

According to the classification provided in<sup>55</sup>, the pressure of UHV varies between  $10^{-8}$  and  $10^{-12}$  mbar while HV pressure range spans from  $10^{-3}$  to  $10^{-8}$  mbar. This means that in the case of  $10^{-6}$  mbar, which is the typical operation pressure of CTOF, the mean free path in HV is  $L_{\text{HV}} \approx 66$  m. In the case of  $10^{-9}$  mbar, which is the typical operation pressure of TOF.SIMS<sup>5</sup> (the pressure increases to  $10^{-6} - 10^{-5}$  mbar when oxygen flooding is provided), the mean free path in UHV is  $L_{\text{UHV}} \approx 66$  km. These values are comparable to the typical  $L_{\text{HV}}$  and  $L_{\text{UHV}}$  reported in the literature<sup>56</sup>. Although  $L_{\text{HV}}$  is shorter than  $L_{\text{UHV}}$  by three orders of magnitude in this case, both values are much greater than the size of TOF-SIMS analytical chambers used in this study.

Another parameter, which is important for the TOF-SIMS analysis, is the time needed to form a single monolayer on a material surface,  $\tau$  (in seconds), which is correlated with pressure<sup>56</sup> by

$$\tau = \frac{2.49 \times 10^{-6}}{p}. \quad (2)$$

This dependency is only valid when a surface is clean and the sticking coefficient, i.e. the probability that an atom/a molecule will stay on a surface after striking it, is unity. The value of the sticking coefficient depends on a material type (very reactive materials, such as alkali metals or rare earth metals, have the sticking coefficient equal, or nearly, to 1 but many other materials have much lower sticking coefficients<sup>57</sup>), temperature and surface coverage<sup>58</sup>. According to Equation 2,  $\tau_{\text{UHV}} \approx 42$  min and  $\tau_{\text{HV}} \approx 2.5$  s in the case of considered UHV and HV pressure values of  $10^{-9}$  mbar and  $10^{-6}$  mbar, respectively. The UHV measurements with TOF.SIMS<sup>5</sup>, which are presented in this work, on average have taken less than 3 minutes per scan. Therefore, in such conditions residual gas molecules had no time to completely cover the sample surface. However, in the case of measurements conducted with CTOF, the dwell time (i.e. the time during which a FIB beam stays on a given pixel of an

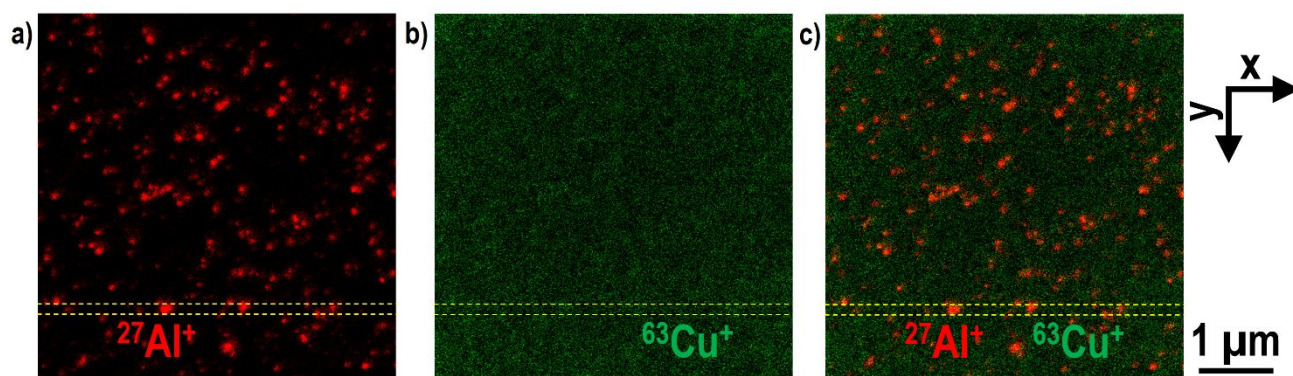


Figure 6. 2D elemental distributions of the sample main isotopes (a)  $^{27}\text{Al}^+$ , b)  $^{63}\text{Cu}^+$ , c) an overlay of  $^{27}\text{Al}^+$  and  $^{63}\text{Cu}^+$  signals) obtained with the  $^{69}\text{Ga}^+$  primary ion beam at HV conditions using the newest CTOF prototype. Integration over the first 35 frames (the region marked with the yellow dashed lines given in Figure S5) was applied to obtain the lateral images. The signal intensity was adjusted individually for each image. The yellow dashed lines denote the region used for side views (Figure S5).

analyzed sample region) of  $10\ \mu\text{s}$  and  $1024 \times 1024$  pixel array (i.e.  $1.05 \times 10^6$  pixels in total) resulted in over 10 s needed to acquire a single scan (the actual scan duration is longer as the imaging beam moves from one pixel to another and from one line to another). This means that gas molecules present in the vacuum chamber potentially had enough time to adsorb on a sample surface and completely cover it. Although this is usually considered as a drawback of HV-based systems, in some cases, it can have beneficial effect as, for example, the presence of oxygen in the vicinity of positively ionizing elements can significantly increase the secondary ion generation.

Figures 6 and S4 show the elemental distribution of the Al nanoparticles buried under Cu thin film obtained with the upgraded HV-compatible prototype of the CTOF detector. Despite higher (when compared to TOF-SIMS<sup>5</sup>) base pressure in the analytical chamber, a very high Al signal was recorded. This allowed Al nanoparticles to be represented in the lateral plane (Figure 6) and in the depth (Figure S5). These results are comparable with the results obtained at UHV. The differences between image quality result not only from the vacuum pressure but also from the type of primary ion beam (a detailed comparison can be found in<sup>27</sup>), applied ion beam energies and currents. Besides, no supplementary gas was delivered to the sample surface during the TOF-SIMS measurement at HV. In this case, it is very likely that the spot size of applied  $^{69}\text{Ga}^+$  primary beam was much smaller than the spot size of  $\text{Bi}_3^{2+}$  beam used during the UHV measurements. This can result in much more accurate representation of Al nanoparticle size and shape. According to<sup>59</sup>, the Ga beam spot size can be as small as 2.5 nm at 1 pA ion current. So far, an operation at such low beam currents was not applicable for TOF-SIMS due to an insufficient secondary ion count rate. However, the recent improvements of the ion extraction and transfer optics of HV-compatible CTOF prototype as well as the better vacuum system and more precise positioning of the sample stage have enabled the chemical measurements to be conducted at only 4 pA primary ion current. Probably, this is also the main reason why the spatial representation of Al nanoparticles presented in this work is much better than in the case of our previous studies<sup>27</sup> on Al nanoparticles distributed in a BMG (i.e. ZrCuAg; conducted at 15 pA ion current). However, the importance of the matrix effect<sup>60,61</sup> cannot be excluded as Cu and ZrCuAg media, in which the Al

nanoparticles were deposited, can affect the Al ionization efficiency in a different manner. Remarkably, in the case of Al nanoparticles buried under the Cu thin film the higher resolution (resulting in the higher quality of elemental images) was achieved despite much lower concentration and size of the Al nanoparticles in the thin film volume.

It is worth mentioning that the evolution of collision events and energy transfer are significantly different in the case of ion beams and cluster ion projectiles<sup>62–65</sup>. This leads to different sample's surface damage, penetration depths as well as sputtering yields and, therefore, influence the quality of chemical images and depth profiles. Figure S6 shows the depth profiles obtained with the  $^{69}\text{Ga}^+$  beam. A peak of  $^{69}\text{Ga}^+$  signal distribution appears close to the interface between the Cu thin film and the Si substrate. Furthermore, signals detected at masses 96 and 132 can indicate formation of  $^{69}\text{Ga}^{27}\text{Al}^+$  and  $^{69}\text{Ga}^{63}\text{Cu}^+$  ions, respectively. These signals' maxima are shifted with respect to the locations of  $^{27}\text{Al}^+$ ,  $^{63}\text{Cu}^+$  and  $^{69}\text{Ga}^+$  signal peaks and, therefore, can potentially suggest the implantation of  $^{69}\text{Ga}^+$  and  $^{69}\text{Ga}^+$ -based ions. However, the assessment of exact locations of these implantations requires molecular dynamics simulations.

#### STEM/EDX elemental analysis on the sample cross-section

The STEM/EDX elemental maps of the sample composition were performed on a sample cross-section (Figure 7). In this measurement type, an area considered for the analysis is much smaller than in the case of in-plane imaging. However, it allows the location of Al nanoparticles to be precisely assessed in depth. The STEM/EDX results confirm that Al nanoparticles formed less than a single monolayer directly located on the Si substrate surface. Moreover, they are spatially separated, i.e. no agglomerates are present, which was one of the main objectives when designing the model sample for verifying the potential of the TOF-SIMS technique. Neither the diffusion of entire Al nanoparticles nor significantly large Al clusters were observed in the measured region. The size of the nanoparticles was not uniform and varied between 19 nm and 36 nm. The largest nanoparticle has a spherical shape but the smaller nanoparticles seem to be smeared towards the substrate. The 52 nm thickness of the Cu thin film was measured. This proves the precision of the PVD technique in the



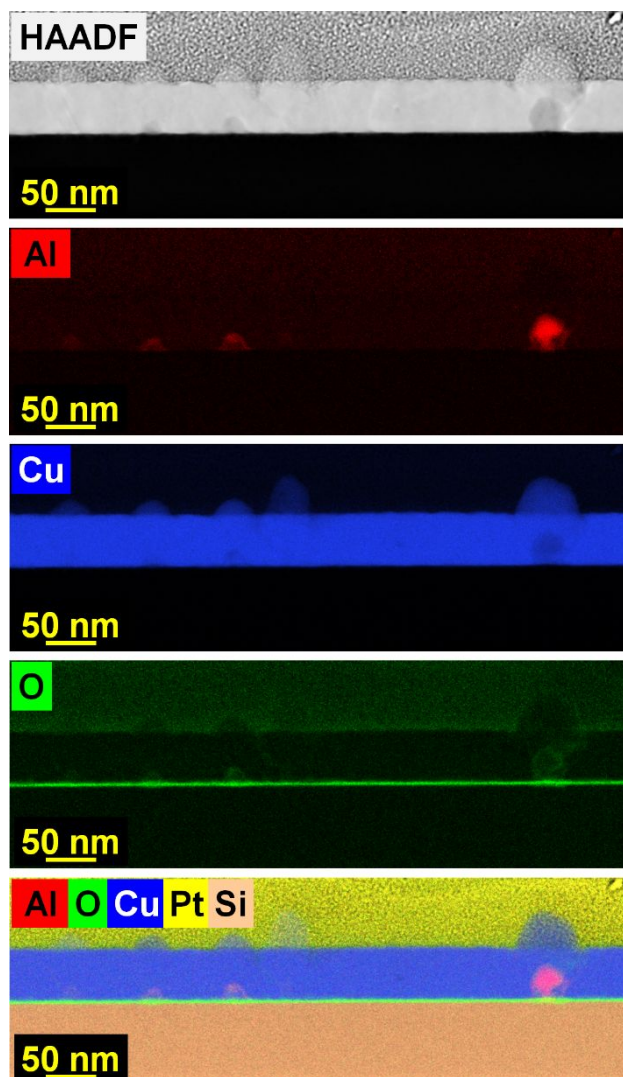


Figure 7. STEM/HAADF and STEM/EDX images of the sample cross-section. The scale in colour maps corresponds to the material quantity (black denotes the minimum value and the most intense colour shows the maximum value).

nanoscale within 4% error margin in this case as the designed thickness of Cu layer was 50 nm. The STEM/EDX results have shown Cu signal deficiency at the location of Al nanoparticles which was not observed in the TOF-SIMS data. Besides, the nanoparticles are confined within the oxidized shells, as expected. Due to the insufficiently low signal, it was not possible to estimate the thickness of these shells. A strong oxygen signal was recorded also on the entire Si substrate surface. The thin film surface was oxidized too but with lower intensity.

In Figure S7 an elemental depth profile of the sample analysis region given in Figure 7 is presented. In this case, the signals are integrated over the lateral plane (i.e. 619 nm length and 124 nm thickness). The locations of the interfaces between the Pt protective layer and the thin film and between the thin film and the Si substrate were estimated based on the cross points between Cu signal distribution with Pt signal distribution and Si signal distribution. The presence of Cu signal within the region of Pt protective layer results from the thin film surface roughness induced by the buried Al nanoparticles. Two O signal peaks were recorded at the interfaces, which confirms the Si substrate surface oxidation and the oxidation of the Cu thin film surface. Within the thin film, Al gives a non-uniformly distributed signal due to

the variations in the Al nanoparticle size. The stronger Al signal is observed close to the Si substrate which is consistent with the design of the model sample. The detection of Al near the thin film surface can indicate the diffusion of Al atoms from the buried Al nanoparticles.

The STEM/EDX provides quantitative information on the sample composition. Moreover, the size of sample components can be assessed with a nanometre scale. However, the analysis region is relatively small and might not be representative for the entire material structure. Besides, the duration and complexity of the sample preparation (which usually requires additional instrumentation such as FIB) remain the main drawbacks of this technique.

#### Comparison of the TOF-SIMS and STEM/EDX techniques

TOF-SIMS and STEM/EDX are alternative elemental characterization techniques. However, the decision which one should be used strongly depends on the main objectives of a study. Certainly, TOF-SIMS has an advantage over STEM/EDX regarding the detection of elements. Both, light and heavy elements can be detected with high mass resolution during a single measurement (however positive and negative ions have to be measured separately). Moreover, TOF-SIMS allows for isotope recognition which can find many applications, especially in medicine and geology. Besides, complex ionized molecules can be measured. Apart from that, a sample can be studied in a wide range of ROI size (without any intermittent steps such as sample preparation) enabling for local and global characterization of a sample chemical structure. This is not attainable for STEM/EDX due to a limited specimen size. Since no particular sample preparation is required prior to TOF-SIMS measurements (preferably a sample should be flat and conductive though), no additional instrumentation is needed (in contrast to STEM/EDX). This reduces the overall experimental duration time. Although TOF-SIMS is a powerful qualitative technique, it does not provide quantitative information (unless dedicated standards are provided, which is not the case regarding novel materials) due to the matrix effect. Therefore, STEM/EDX has to be used when the knowledge of exact sample chemical composition is needed. Besides, STEM/EDX is also much more precise regarding the size measurements of nano-objects (which can be performed on the atomic level) as TOF-SIMS images in the nanoscale can represent a convolution of an imaged object and a shape of imaging primary ion beam<sup>66</sup>. Apart from principal differences, the HV-compatible TOF-SIMS detectors can be combined within the same analytical chamber with techniques such as SEM, EDX, WDXS (Wavelength-Dispersive X-ray Spectroscopy), AFM, EBSD, Raman Spectroscopy and GIS (Gas Injection System). This allows correlative sample characterization to be conducted *in situ* without breaking vacuum conditions. A detailed comparison of the TOF-SIMS and STEM/EDX methods is provided in Table 1.

#### CONCLUSIONS

The intense development of nanoparticle-based technologies demands reliable and efficient characterization techniques to maximize the

**Table 1. Comparison of TOF-SIMS and STEM/EDX techniques.**

		TOF-SIMS	STEM/EDX
Physical principle		Detection of secondary ions <sup>23</sup>	Detection of electrons (STEM) and characteristic X-rays (EDX) <sup>25,26</sup>
Detection of elements		All ionized	Elements with $Z \geq 4$ <sup>67,68,a)</sup>
Isotope recognition		Yes	No
Imaging inorganic and organic molecules		Yes <sup>27,65,69-73</sup>	No
Data representation		3D <sup>27,69,74</sup>	2D <sup>b)</sup>
Highest resolution	Lateral	< 20 nm <sup>73</sup>	0.1 nm <sup>75</sup>
	Depth	< 1 nm <sup>76</sup>	<10 nm <sup>77,c)</sup>
Typical 2D ROI size		1 – 10 <sup>4</sup> μm <sup>2</sup>	10 <sup>-4</sup> – 10 <sup>2</sup> μm <sup>2</sup>
Quantification		No <sup>d)</sup>	Yes
Sample preparation		None <sup>e), f)</sup>	Lift-out <sup>37,49</sup> , cross-section <sup>49</sup> , plan view <sup>49</sup>
Additional instrumentation		None <sup>g)</sup>	FIB <sup>50</sup> with GIS <sup>78, h)</sup> and micromanipulator
Origin of potential artefacts		Mass interference <sup>74,79,80</sup> , matrix effect <sup>60,61,81</sup> , different sputtering rates of sample components <sup>82</sup> , topology <sup>37,53</sup> , FIB curtaining <sup>83</sup>	Sum peaks <sup>84</sup> , escape peaks <sup>84</sup> , coherent bremsstrahlung peaks <sup>84</sup> , absorption <sup>84</sup> , fluorescence, generation of X-rays from Si detector <sup>84</sup> , peak overlaps <sup>85</sup> , FIB curtaining
Measurement type		Destructive	Destructive <sup>i)</sup>

<sup>a)</sup>Problematic for elements with  $4 \leq Z \leq 10$  <sup>86</sup>, <sup>b)</sup>usually STEM/EDX measurements are conducted in 2D space but 3D tomography is possible as well<sup>87</sup>, <sup>c)</sup>this value refers to the thinnest TEM lamellae, <sup>d)</sup>quantification is not possible in the case of samples with unknown composition; in some cases standards can be used for attempting the quantitative results, <sup>e)</sup>sample surface should be flat<sup>88</sup>; <sup>f)</sup>in some cases samples are coated with thin Au or C layers to prevent charge collection on the sample surface, <sup>g)</sup>a sputter coater is needed for Au or C thin film deposition; GIS can be used for TOF-SIMS signal enhancement<sup>80,89</sup>, <sup>h)</sup>GIS is needed for depositing a protective (for example Pt) layer and for a sample lift-out, <sup>i)</sup>the sample lift-out is destructive but a lamellae can be measured multiple times.

functionality of novel systems and to optimize fabrication processes. Moreover, the effect of nanoparticles on living organisms and potential biohazards have to be profoundly examined. This can be achieved by the STEM/EDX and TOF-SIMS techniques which enable a sample composition to be characterized with nanoscale resolution.

In this work, the potential and limitations of TOF-SIMS and STEM/EDX were compared based on the results obtained with the novel dedicated model sample consisting of low-concentration 10s of nanometer large Al nanoparticles buried under the 50 nm thick Cu thin film. The TOF-SIMS capability to spatially resolve individual nanoparticles was demonstrated under UHV and HV. This was a great achievement especially taking into account the very small Al content in the studied specimen. Remarkably, the imaging of nanoparticles with such high lateral resolution using the HV-compatible TOF detector was obtained for the first time. This was possible thanks to operation at a very low primary ion beam current of 4 pA (which approaches the conditions of 1 pA providing the smallest possible Ga<sup>+</sup> beam spot size of 2.5 nm<sup>59</sup>) as well as the upgraded ion extraction and transfer optics of the new CTOF prototype. Moreover, it was proven that the measured Al signal represents real chemical distribution and is not a result of topology artefacts induced by the sample surface roughness. Undoubtedly, the high ionization of Al played a crucial role in the success of our studies. However, the recent development of gas-assisted TOF-SIMS<sup>80,89</sup>, which (in the case of some metals and alloys) demonstrates the great potential for enhancing

secondary ion generation, is very promising for detecting and chemically imaging weakly ionizing elements.

TOF-SIMS is a competing and alternative technique to STEM/EDX, which currently is the most frequently used tool for elemental characterization at the nanoscale. Both methods have different pros and cons. Therefore, the choice of the technique strongly depends on the main objectives of a study, such as the possibility of detecting all ionized elements and molecules, chemical representation in 3D, precise measurement of nano-object size or dimensions of the chemical system. Moreover, time-constraints as well as an access to the additional sample preparation instrumentation or the possibility of conducting correlative measurements *in situ* can be decisive. The provided detailed comparisons of the TOF-SIMS and STEM/EDX characteristics can serve as guidelines for finding the most optimal solution for efficient investigation of nano-systems.

## AUTHOR INFORMATION

### Corresponding Author

\* agnieszka.priebe@empa.ch

## ACKNOWLEDGEMENTS

This project has received funding from the EU-H2020 research and innovation programme under grant agreement No 654360 having benefitted from the access provided by CEA-LETI in Grenoble (France) within the framework of the NFFA-Europe Transnational Access Activity. The EMPAPOSTDOCS-II programme has received funding from the European Union's Horizon 2020 research and innovation programme under the Marie Skłodowska-Curie



grant agreement number 754364. The authors thank TOFWERK (Thun, Switzerland) for the access to the experimental site and the possibility of using the newest prototype of the CTOF detector.

## ASSOCIATED CONTENT

### Supporting information:

Figure S1. Diagram of the deposition setup.

Figure S2. The size distribution of Al nanoparticles measured with a quadrupole mass spectrometer.

Figure S3. TOF-SIMS depth profiles of Al nanoparticles buried under Cu thin film obtained with Bi<sub>3</sub><sup>2+</sup> beam.

Figure S4. The topology of the sample surface imaged with SEM.

Figure S5. 2D side views (in depth) of the sample main isotopes: <sup>27</sup>Al<sup>+</sup>, <sup>63</sup>Cu<sup>+</sup>, <sup>28</sup>Si<sup>+</sup> and their overlay obtained with the <sup>69</sup>Ga<sup>+</sup> beam.

Figure S6. TOF-SIMS depth profiles of Al nanoparticles buried under Cu thin film obtained with Ga<sup>+</sup> beam.

Figure S7. STEM/EDX depth profiles.

## REFERENCES

- (1) Baker, C.; Pradhan, A.; Pakstis, L.; Pochan, D. J.; Shah, S. I. Synthesis and Antibacterial Properties of Silver Nanoparticles. *J. Nanosci. Nanotechnol.* **2005**, *5* (2), 244–249. <https://doi.org/10.1166/jnn.2005.034>.
- (2) Panáček, A.; Kolář, M.; Večeřová, R.; Pucek, R.; Soukupová, J.; Kryštof, V.; Hamal, P.; Zbořil, R.; Kvítek, L. Antifungal Activity of Silver Nanoparticles against *Candida* Spp. *Biomaterials* **2009**, *30* (31), 6333–6340. <https://doi.org/10.1016/j.biomaterials.2009.07.065>.
- (3) Lara, H. H.; Ayala-Núñez, N. V.; Ixtapan-Turrent, L.; Rodríguez-Padilla, C. Mode of Antiviral Action of Silver Nanoparticles against HIV-1. *J. Nanobiotechnology* **2010**, *8*, 1–10. <https://doi.org/10.1186/1477-3155-8-1>.
- (4) Roe, D.; Karandikar, B.; Bonn-Savage, N.; Gibbins, B.; Rouillet, J. baptiste. Antimicrobial Surface Functionalization of Plastic Catheters by Silver Nanoparticles. *J. Antimicrob. Chemother.* **2008**, *61* (4), 869–876. <https://doi.org/10.1093/jac/dkn034>.
- (5) Zeng, S.; Yong, K. T.; Roy, I.; Dinh, X. Q.; Yu, X.; Luan, F. A Review on Functionalized Gold Nanoparticles for Biosensing Applications. *Plasmonics* **2011**, *6* (3), 491–506. <https://doi.org/10.1007/s11468-011-9228-1>.
- (6) Ilić, V.; Šaponjić, Z.; Vodnik, V.; Mihailović, D.; Jovančić, P.; Nedeljković, J.; Radetić, M. The Study of Coloration and Antibacterial Efficiency of Corona Activated Dyed Polyamide and Polyester Fabrics Loaded with Ag Nanoparticles. *Fibers Polym.* **2009**, *10* (5), 650–656. <https://doi.org/10.1007/s12221-010-0650-3>.
- (7) Paik, H.; Choi, Y. Y.; Hong, S.; No, K. Effect of Ag Nanoparticle Concentration on the Electrical and Ferroelectric Properties of Ag/P(VDF-TrFE) Composite Films. *Sci. Rep.* **2015**, *5* (January), 1–7. <https://doi.org/10.1038/srep13209>.
- (8) Alshehri, A. H.; Jakubowska, M.; Młoziniak, A.; Horaczek, M.; Rudka, D.; Free, C.; Carey, J. D. Enhanced Electrical Conductivity of Silver Nanoparticles for High Frequency Electronic Applications. *ACS Appl. Mater. Interfaces* **2012**, *4* (12), 7007–7010. <https://doi.org/10.1021/am3022569>.
- (9) Cui, W.; Lu, W.; Zhang, Y.; Lin, G.; Wei, T.; Jiang, L. Gold Nanoparticle Ink Suitable for Electric-Conductive Pattern Fabrication Using in Ink-Jet Printing Technology. *Colloids Surfaces A Physicochem. Eng. Asp.* **2010**, *358* (1–3), 35–41. <https://doi.org/10.1016/j.colsurfa.2010.01.023>.
- (10) Shen, W.; Zhang, X.; Huang, Q.; Xu, Q.; Song, W. Preparation of Solid Silver Nanoparticles for Inkjet Printed Flexible Electronics with High Conductivity. *Nanoscale* **2014**, *6* (3), 1622–1628. <https://doi.org/10.1039/c3nr05479a>.
- (11) Huang, Y. F.; Lin, Y. W.; Lin, Z. H.; Chang, H. T. Aptamer-Modified Gold Nanoparticles for Targeting Breast Cancer Cells through Light Scattering. *J. Nanoparticle Res.* **2009**, *11* (4), 775–783. <https://doi.org/10.1007/s11051-008-9424-x>.
- (12) Gearheart, L. A.; Ploehn, H. J.; Murphy, C. J. Oligonucleotide Adsorption to Gold Nanoparticles: A

Surface-Enhanced Raman Spectroscopy Study of Intrinsically Bent DNA. *J. Phys. Chem. B* **2001**, *105* (50), 12609–12615. <https://doi.org/10.1021/jp0106606>.

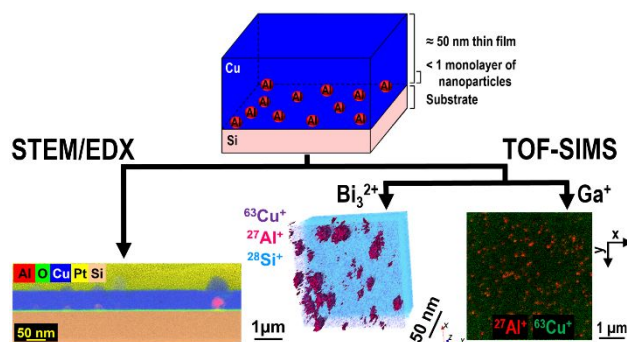
- (13) Kneipp, J.; Kneipp, H.; Rice, W. L.; Kneipp, K. Optical Probes for Biological Applications Based on Surface-Enhanced Raman Scattering from Indocyanine Green on Gold Nanoparticles. *Anal. Chem.* **2005**, *77* (8), 2381–2385. <https://doi.org/10.1021/ac050109v>.
- (14) Nath, N.; Chilkoti, A. Label-Free Biosensing by Surface Plasmon Resonance of Nanoparticles on Glass: Optimization of Nanoparticle Size. *Anal. Chem.* **2004**, *76* (18), 5370–5378. <https://doi.org/10.1021/ac049741z>.
- (15) Liu, J.; Lu, Y. Accelerated Color Change of Gold Nanoparticles Assembled by DNAzymes for Simple and Fast Colorimetric Pb<sup>2+</sup> Detection. *J. Am. Chem. Soc.* **2004**, *126* (39), 12298–12305. <https://doi.org/10.1021/jao46628h>.
- (16) Liu, C. W.; Hsieh, Y. T.; Huang, C. C.; Lin, Z. H.; Chang, H. T. Detection of Mercury(II) Based on Hg<sub>2</sub><sup>+</sup>-DNA Complexes Inducing the Aggregation of Gold Nanoparticles. *Chem. Commun.* **2008**, No. 19, 2242–2244. <https://doi.org/10.1039/b719856f>.
- (17) Zhang, S.; Wang, N.; Yu, H.; Niu, Y.; Sun, C. Covalent Attachment of Glucose Oxidase to an Au Electrode Modified with Gold Nanoparticles for Use as Glucose Biosensor. *Bioelectrochemistry* **2005**, *67* (1), 15–22. <https://doi.org/10.1016/j.bioelechem.2004.12.002>.
- (18) Rasmussen, J. W.; Martinez, E.; Louka, P.; Wingett, D. G. Zinc Oxide Nanoparticles for Selective Destruction of Tumor Cells and Potential for Drug Delivery Applications. *Expert Opin. Drug Deliv.* **2010**, *7* (9), 1063–1077. <https://doi.org/10.1517/17425247.2010.502560>.
- (19) Kubota, Y.; Shuin, T.; Kawasaki, C.; Hosaka, M.; Kitamura, H.; Cai, R.; Sakai, H.; Hashimoto, K.; Fujishima, A. Photokilling of T-24 Human Bladder Cancer Cells with Titanium Dioxide. *Br. J. Cancer* **1994**, *70*, 1107–1111.
- (20) Raj, S.; Jose, S.; Sumod, U. S.; Sabitha, M. Nanotechnology in Cosmetics: Opportunities and Challenges. *J. Pharm. Bioallied Sci.* **2012**, *4* (3), 186–193. <https://doi.org/10.4103/0975-7406.99016>.
- (21) Torabi, Z.; Mohammadi Nafchi, A. The Effects of SiO<sub>2</sub> Nanoparticles on Mechanical and Physicochemical Properties of Potato Starch Films. *J. Chem. Heal. Risks* **2013**, *3* (1), 33–42.
- (22) Park, B.; Donaldson, K.; Duffin, R.; Tran, L.; Kelly, F.; Mudway, I.; Morin, J. P.; Guest, R.; Jenkinson, P.; Samarasekera, Z.; et al. Hazard and Risk Assessment of a Nanoparticulate Cerium Oxide-Based Diesel Fuel Additive - A Case Study. *Inhal. Toxicol.* **2008**, *20* (6), 547–566. <https://doi.org/10.1080/08958370801915309>.
- (23) Benninghoven, A.; Rudenauer, F. G.; Werner, H. W. Secondary Ion Mass Spectrometry—Basic Concepts, Instrumental Aspects, Applications and Trends. *Surf. Interface Anal.* **1987**, *10* (8), 435. <https://doi.org/10.1002/sia.740100811>.
- (24) Heide, P. van der. *Secondary Ion Mass Spectrometry*; John Wiley & Sons, Inc.: Hoboken, NJ, USA, 2014. <https://doi.org/10.1002/9781118916780.fmatter>.
- (25) Williams, D. B.; Carter, C. B. The Transmission Electron Microscope. In *Transmission Electron Microscopy*; 1996. [https://doi.org/10.1007/978-1-4757-2519-3\\_1](https://doi.org/10.1007/978-1-4757-2519-3_1).
- (26) Reimer, L.; Kohl, H. *Transmission Electron Microscopy Physics of Image Formation*; 2008. <https://doi.org/10.1007/978-0-387-34758-5>.
- (27) Priebe, A.; Barnes, J.-P.; Edwards, T. E. J.; Pethö, L.; Balogh, I.; Michler, J. 3D Imaging of Nanoparticles in an Inorganic Matrix Using TOF-SIMS Validated with STEM and EDX. *Anal. Chem.* **2019**, *91*, 11834–11839. Article. <https://doi.org/10.1021/acs.analchem.9b02545>.
- (28) Wang, W. H.; Dong, C.; Shek, C. H. Bulk Metallic Glasses. *Mater. Sci. Eng. R Reports* **2004**, *44* (2–3), 45–90. <https://doi.org/10.1016/j.mser.2004.03.001>.
- (29) Benninghoven, A. Chemical Analysis of Inorganic and Organic Surfaces and Thin Films by Static Time-of-Flight Secondary Ion Mass Spectrometry (TOF-SIMS). *ChemInform* **1994**, No. 33, 1023. <https://doi.org/10.1002/chin.199437319>.
- (30) Temple, T. L.; Bagnall, D. M. Optical Properties of Gold and Aluminium Nanoparticles for Silicon Solar Cell

- Applications. *J. Appl. Phys.* **2011**, *109* (8). <https://doi.org/10.1063/1.3574657>.
- (31) Hylton, N. P.; Li, X. F.; Giannini, V.; Lee, K. H.; Ekins-Daukes, N. J.; Loo, J.; Vercruysee, D.; Van Dorpe, P.; Sodabanlu, H.; Sugiyama, M.; et al. Loss Mitigation in Plasmonic Solar Cells: Aluminium Nanoparticles for Broadband Photocurrent Enhancements in Gaas Photodiodes. *Sci. Rep.* **2013**, *3*, 1–6. <https://doi.org/10.1038/srep02874>.
- (32) Zhou, L.; Tan, Y.; Wang, J.; Xu, W.; Yuan, Y.; Cai, W.; Zhu, S.; Zhu, J. 3D Self-Assembly of Aluminium Nanoparticles for Plasmon-Enhanced Solar Desalination. *Nat. Photonics* **2016**, *10* (6), 393–398. <https://doi.org/10.1038/nphoton.2016.75>.
- (33) Lozano, G.; Grzela, G.; Verschuuren, M. A.; Ramezani, M.; Rivas, J. G. Tailor-Made Directional Emission in Nanoimprinted Plasmonic-Based Light-Emitting Devices. *Nanoscale* **2014**, *6* (15), 9223–9229. <https://doi.org/10.1039/c4nr01391c>.
- (34) Tyagi, H.; Phelan, P. E.; Prasher, R.; Peck, R.; Lee, T.; Pacheco, J. R.; Arentzen, P. Increased Hot-Plate Ignition Probability for Nanoparticle-Laden Diesel Fuel. *Nano Lett.* **2008**, *8* (5), 1410–1416. <https://doi.org/10.1021/nl80277d>.
- (35) Schmitz, C. J. *Handbook of Aluminium Recycling*; Vulkan-Verlag GmbH: Essen, Germany, 2006.
- (36) Vickermann, J. C.; Briggs, D. *ToF-SIMS: Materials Analysis by Mass Spectrometry*, 2nd ed.; IM Publications LLP: West Sussex, United Kingdom, 2013.
- (37) Priebe, A.; Audoit, G.; Barnes, J. P. A Novel PFIB Sample Preparation Protocol for Correlative 3D X-Ray CNT and FIB-TOF-SIMS Tomography. *Ultramicroscopy* **2017**, *173*, 10–13. <https://doi.org/10.1016/j.ultramic.2016.11.010>.
- (38) Nguyen, L.; Hashimoto, T.; Zakharov, D. N.; Stach, E. A.; Rooney, A. P.; Berkels, B.; Thompson, G. E.; Haigh, S. J.; Burnett, T. L. Atomic-Scale Insights into the Oxidation of Aluminum. *ACS Appl. Mater. Interfaces* **2018**, *10* (3), 2230–2235. <https://doi.org/10.1021/acsami.7b17224>.
- (39) Evertsson, J.; Bertram, F.; Zhang, F.; Rullik, L.; Merte, L. R.; Shipilin, M.; Soldemo, M.; Ahmadi, S.; Vinogradov, N.; Carlà, F.; et al. The Thickness of Native Oxides on Aluminum Alloys and Single Crystals. *Appl. Surf. Sci.* **2015**, *349*, 826–832. <https://doi.org/10.1016/j.apsusc.2015.05.043>.
- (40) Jeurgens, L.; Sloof, W.; Tichelaar, F.; Mittemeijer, E. Thermodynamic Stability of Amorphous Oxide Films on Metals: Application to Aluminum Oxide Films on Aluminum Substrates. *Phys. Rev. B - Condens. Matter Mater. Phys.* **2000**, *62* (7), 4707–4719. <https://doi.org/10.1103/PhysRevB.62.4707>.
- (41) Cai, N.; Zhou, G.; Müller, K.; Starr, D. E. Effect of Oxygen Gas Pressure on the Kinetics of Alumina Film Growth during the Oxidation of Al(111) at Room Temperature. *Phys. Rev. B - Condens. Matter Mater. Phys.* **2011**, *84* (12), 1–6. <https://doi.org/10.1103/PhysRevB.84.125445>.
- (42) Zheng, Y. T.; He, M.; Cheng, G. xu; Zhang, Z.; Xuan, F. Z.; Wang, Z. Effect of Ionization on the Oxidation Kinetics of Aluminum Nanoparticles. *Chem. Phys. Lett.* **2018**, *696*, 8–11. <https://doi.org/10.1016/j.cplett.2018.02.039>.
- (43) Dumas, P.; Dubarry-Barbe, J. P.; Riviere, D.; Levy, Y.; Corset, J. Growth of Thin Alumina Film on Aluminium At Room Temperature: A Kinetic and Spectroscopic Study By Surface Plasmon Excitation. *J. Phys. (Paris), Colloq.* **1983**, *44* (12), 205–208. <https://doi.org/10.1051/jphyscol:19831042>.
- (44) Campbell, T.; Kalia, R. K.; Nakano, A.; Vashishta, P.; Ogata, S.; Rodgers, S. Dynamics of Oxidation of Aluminum Nanoclusters Using Variable Charge Molecular-Dynamics Simulations on Parallel Computers. *Phys. Rev. Lett.* **1999**, *82* (24), 4866–4869. <https://doi.org/10.1103/PhysRevLett.82.4866>.
- (45) Novikov, S. M.; Popok, V. N.; Evlyukhin, A. B.; Hanif, M.; Morgen, P.; Fiutowski, J.; Beermann, J.; Rubahn, H. G.; Bozhevolnyi, S. I. Highly Stable Monocrystalline Silver Clusters for Plasmonic Applications. *Langmuir* **2017**, *33* (24), 6062–6070. <https://doi.org/10.1021/acs.langmuir.7b00772>.
- (46) Sree Harsha, K. S. *Principles of Vapor Deposition of Thin Films*; Elsevier Science: Oxford, UK, 2006. <https://doi.org/10.1016/B978-008044699-8/50005-X>.
- (47) Hartmann, H.; Popok, V. N.; Barke, I.; Von Oeynhausen, V.; Meiwes-Broer, K. H. Design and Capabilities of an Experimental Setup Based on Magnetron Sputtering for Formation and Deposition of Size-Selected Metal Clusters on Ultra-Clean Surfaces. *Rev. Sci. Instrum.* **2012**, *83* (7). <https://doi.org/10.1063/1.4732821>.
- (48) Huttel, Y. *Gas-Phase Synthesis of Nanoparticles*; Wiley-VCH Verlag: Weinheim, Germany, 2017. <https://doi.org/10.1002/9783527698417>.
- (49) Giannuzzi, L. A.; Stevie, F. A. A Review of Focused Ion Beam Milling Techniques for TEM Specimen Preparation. *Micron* **1999**, *30* (3), 197–204. [https://doi.org/10.1016/S0968-4328\(99\)00005-0](https://doi.org/10.1016/S0968-4328(99)00005-0).
- (50) Giannuzzi, L. A.; Stevie, F. A. *Introduction to Focused Ion Beams Instrumentation, Theory, Techniques and Practice*; Springer: New York, 2005.
- (51) Binning, G.; Quate, C.; Gerber, C. Atomic Force Microscope. *Phys. Rev. Lett.* **1986**, *56* (9), 930–933. <https://doi.org/10.1103/PhysRevLett.56.930>.
- (52) Yamamura, Y.; Tawara, H. ENERGY DEPENDENCE OF ION-INDUCED SPUTTERING YIELDS FROM MONATOMIC SOLIDS AT NORMAL INCIDENCE. *At. Data Nucl. Data Tables* **1996**, *62* (2), 149–253. <https://doi.org/10.1006/ADND.1996.0005>.
- (53) Lee, J. L. S.; Gilmore, I. S.; Fletcher, I. W.; Seah, M. P. Topography and Field Effects in the Quantitative Analysis of Conductive Surfaces Using ToF-SIMS. *Appl. Surf. Sci.* **2008**, *255* (4), 1560–1563. <https://doi.org/10.1016/j.apsusc.2008.05.164>.
- (54) Whitby, J. A.; Östlund, F.; Horvath, P.; Gabureac, M.; Riestner, J. L.; Utke, I.; Hohl, M.; Sedláček, L.; Jiruše, J.; Friedli, V.; et al. High Spatial Resolution Time-of-Flight Secondary Ion Mass Spectrometry for the Masses: A Novel Orthogonal ToF FIB-SIMS Instrument with in Situ AFM. *Adv. Mater. Sci. Eng.* **2012**, *2012*. <https://doi.org/10.1155/2012/180437>.
- (55) O'Hanlon, J. F. *A User's Guide to Vacuum Technology*, 3rd ed.; Wiley & Sons, Inc: New Jersey, 2003.
- (56) Berman, A. *Vacuum Engineering Calculations, Formulas, and Solved Exercises*; Academic Press: San Diego, USA, 1992.
- (57) Hüfner, S. *Photoelectron Spectroscopy: Principles and Applications*; Springer-Verlag Berlin Heidelberg: Berlin, 2003.
- (58) Smith, T. Effect of Surface Coverage and Temperature on the Sticking Coefficient. *J. Chem. Phys.* **1964**, *40* (7), 1805–1812. <https://doi.org/10.1063/1.1725409>.
- (59) Fleck, R. A.; Humbel, B. M. *Biological Field Emission Scanning Electron Microscopy*; John Wiley & Sons, INC.: West Sussex, United Kingdom, 2019.
- (60) Deline, V. R.; Katz, W.; Evans, C. A.; Williams, P. Mechanism of the SIMS Matrix Effect. *Appl. Phys. Lett.* **1978**, *33* (9), 832–835. <https://doi.org/10.1063/1.90546>.
- (61) Priebe, A.; Xie, T.; Bürki, G.; Pethö, L.; Michler, J. Matrix Effect in TOF-SIMS Analysis of Two-Element Inorganic Thin Films. *J. Anal. At. Spectrom.* **2020**, *35*, 1156–1166. <https://doi.org/10.1039/C9JA00428A>.
- (62) Postawa, Z.; Czerwinski, B.; Szweczyk, M.; Smiley, E. J.; Winograd, N.; Garrison, B. J. Enhancement of Sputtering Yields Due to C60 versus Ga Bombardment of Ag(111) as Explored by Molecular Dynamics Simulations. *Anal. Chem.* **2003**, *75* (17), 4402–4407. <https://doi.org/10.1021/ac034387a>.
- (63) Postawa, Z.; Czerwinski, B.; Szweczyk, M.; Smiley, E. J.; Winograd, N.; Garrison, B. J. Microscopic Insights into the Sputtering of Ag(111) Induced by C 60 and Ga Bombardment. *J. Phys. Chem. B* **2004**, *108* (23), 7831–7838. <https://doi.org/10.1021/jp049936a>.
- (64) Muramoto, S.; Brison, J.; Castner, D. G. Exploring the Surface Sensitivity of ToF-SIMS by Measuring the Implantation and Sampling Depths of Bin and C60 Ions in Organic Films. *Anal. Chem.* **2012**, *84*, 365–372. <https://doi.org/10.1021/ac202713k>.
- (65) Pillatsch, L.; Östlund, F.; Michler, J. FIBSIMS: A Review of Secondary Ion Mass Spectrometry for Analytical Dual Beam Focussed Ion Beam Instruments. *Prog. Cryst. Growth Charact. Mater.* **2019**, *65* (1), 1–19. <https://doi.org/10.1016/j.pcrysgrow.2018.10.001>.

- (66) Senoner, M.; Wirth, T.; Unger, W. E. S. Imaging Surface Analysis: Lateral Resolution and Its Relation to Contrast and Noise. *J. Anal. At. Spectrom.* **2010**, *25* (9), 1440–1452. <https://doi.org/10.1039/c004323k>.
- (67) Makhlof, A. S. H.; Aliofkhazraei, M. *Handbook of Materials Failure Analysis with Case Studies from the Aerospace and Automotive Industries*, 1st ed.; Butterworth-Heinemann: Oxford, UK, 2015.
- (68) Batchelor, A. W.; Loh, N. L.; Chandrasekaran, M. *Materials Degradation and Its Control by Surface Engineering*, 3rd ed.; Imperial College Press: London, UK, 2011. <https://doi.org/https://doi.org/10.1142/p689>.
- (69) Priebe, A.; Goret, G.; Bleuet, P.; Audoit, G.; Laurencin, J.; Barnes, J. P. 3D Correlative Morphological and Elemental Characterization of Materials at the Deep Submicrometre Scale. *J. Microsc.* **2016**, *264* (2), 247–251. <https://doi.org/10.1111/jmi.12458>.
- (70) Sastre, J.; Lin, T.-Y.; Filippin, A. N.; Priebe, A.; Avancini, E.; Michler, J.; Tiwari, A. N.; Romanyuk, Y. E.; Buecheler, S. Aluminum-Assisted Densification of Cosputtered Lithium Garnet Electrolyte Films for Solid-State Batteries. *ACS Appl. Energy Mater.* **2019**, *acsam.9b01387*. <https://doi.org/10.1021/acsam.9b01387>.
- (71) Bich, C.; Havelund, R.; Moellers, R.; Touboul, D.; Kollmer, F.; Niehuis, E.; Gilmore, I. S.; Brunelle, A. Argon Cluster Ion Source Evaluation on Lipid Standards and Rat Brain Tissue Samples. *Anal. Chem.* **2013**, *85* (16), 7745–7752. <https://doi.org/10.1021/ac4009513>.
- (72) Kubicek, M.; Holzlechner, G.; Opitz, A. K.; Larisegger, S.; Hutter, H.; Fleig, J. A Novel ToF-SIMS Operation Mode for Sub 100 Nm Lateral Resolution: Application and Performance. *Appl. Surf. Sci.* **2014**, *289*, 407–416. <https://doi.org/10.1016/j.apsusc.2013.10.177>.
- (73) Kollmer, F.; Paul, W.; Krehl, M.; Niehuis, E. Ultra High Spatial Resolution SIMS with Cluster Ions - Approaching the Physical Limits. *Surf. Interface Anal.* **2013**, *45* (1), 312–314. <https://doi.org/10.1002/sia.5093>.
- (74) Priebe, A.; Bleuet, P.; Goret, G.; Laurencin, J.; Montinaro, D.; Barnes, J.-P. State-of-the-Art Three-Dimensional Chemical Characterization of Solid Oxide Fuel Cell Using Focused Ion Beam Time-of-Flight Secondary Ion Mass Spectrometry Tomography. *Microsc. Microanal.* **2016**, *22*, 1261–1269. <https://doi.org/10.1017/S1431927616012502>.
- (75) Smith, D. J. Ultimate Resolution in the Electron Microscope? *Mater. Today* **2008**, *11* (SUPPL.), 30–38. [https://doi.org/10.1016/S1369-7021\(09\)70005-7](https://doi.org/10.1016/S1369-7021(09)70005-7).
- (76) <https://www.iontof.com/tof-sims-secondary-ion-mass-spectrometry.html>.
- (77) Lechner, L.; Biskupek, J.; Kaiser, U. Improved Focused Ion Beam Target Preparation of (S)TEM Specimen—a Method for Obtaining Ultrathin Lamellae. *Microsc. Microanal.* **2012**, *18* (2), 379–384. <https://doi.org/10.1017/S1431927611012499>.
- (78) Wang, Z. M. *FIB Nanostructures*; Springer: Heidelberg, 2013.
- (79) Stephan, T. TOF-SIMS in Cosmochemistry. *Planet. Space Sci.* **2001**, *49* (9), 859–906. [https://doi.org/10.1016/S0032-0633\(01\)00037-X](https://doi.org/10.1016/S0032-0633(01)00037-X).
- (80) Priebe, A.; Pethö, L.; Michler, J. Fluorine Gas Coinjection as a Solution for Enhancing Spatial Resolution of Time-of-Flight Secondary Ion Mass Spectrometry and Separating Mass Interference. *Anal. Chem.* **2020**, *92*, 2121–2129. <https://doi.org/https://doi.org/10.1021/acs.analchem.9b04647>.
- (81) Benninghoven, A. Surface Analysis by Secondary Ion Mass Spectrometry (SIMS). *Surf. Sci.* **1994**, *299–300* (C), 246–260. [https://doi.org/10.1016/0039-6028\(94\)90658-0](https://doi.org/10.1016/0039-6028(94)90658-0).
- (82) Henss, A.; Otto, S.-K.; Schaepe, K.; Pauksch, L.; Lips, K. S.; Rohnke, M. High Resolution Imaging and 3D Analysis of Ag Nanoparticles in Cells with ToF-SIMS and Delayed Extraction. *Biointerphases* **2018**, *13* (3), 03B410. <https://doi.org/10.1116/1.5015957>.
- (83) Kwakman, L.; Franz, G.; Taklo, M. M. V.; Klumpp, A.; Ramm, P. Characterization and Failure Analysis of 3D Integrated Systems Using a Novel Plasma-FIB System. *AIP Conf. Proc.* **2011**, *1395* (November), 269–273. <https://doi.org/10.1063/1.3657902>.
- (84) Stolojan, V. *Nanometrology Using the Transmission Electron Microscope*; Morgan & Claypool Publishers: Bristol, UK, 2015.
- (85) West, A. R. *Solid State Chemistry and Its Applications*, 2nd ed.; Wiley & Sons, Ltd: West Sussex, United Kingdom, 2014.
- (86) Marshall, J. L. *Solder Joint Reliability: Theory and Applications*; Lau, J. H., Ed.; Springer Science & Business Media: New York, 1991.
- (87) Slater, T. J. A.; Janssen, A.; Camargo, P. H. C.; Burke, M. G.; Zaluzec, N. J.; Haigh, S. J. STEM-EDX Tomography of Bimetallic Nanoparticles: A Methodological Investigation. *Ultramicroscopy* **2016**, *162*, 61–73. <https://doi.org/10.1016/j.ultramic.2015.10.007>.
- (88) Sodhi, R. N. S. Time-of-Flight Secondary Ion Mass Spectrometry (TOF-SIMS):—Versatility in Chemical and Imaging Surface Analysis. *Analyst* **2004**, *129*, 483–487. <https://doi.org/10.1039/B402607C>.
- (89) Priebe, A.; Utke, I.; Pethö, L.; Michler, J. Application of a Gas-Injection System during the FIB-TOF-SIMS Analysis - Influence of Water Vapor and Fluorine Gas on Secondary Ion Signals and Sputtering Rates. *Anal. Chem.* **2019**, *91* (18), 11712–11722. <https://doi.org/10.1021/acs.analchem.9b02287>.



For Table of Contents only



The comparison of Time-of-Flight Secondary Ion Mass Spectrometry (TOF-SIMS) and Scanning Transmission Electron Microscope combined with Energy-Dispersive X-ray Spectroscopy (STEM/EDX), currently the most powerful elemental characterization techniques in the nanoscale, is presented using a novel model sample consisting of Al nanoparticles buried under a 50 nm thick Cu thin film.